Nano Research

Open Access

Research Article

Integrated trilayer nanofiber membrane with tailored antibacterial, antioxidant, and mechanical properties for accelerated infected wound healing

Huixin Zhang[1,§], Hao Hang[2,§], Youyi Liu[3], Wenjing Cui[1], Junxian An[1], Yan Zhu[2], Han Zhu[1]✉, Mingliang Du[1]✉, Chanyuan Jin[4]✉, and Jianfeng Huang[2]✉

[1] *Key Laboratory of Synthetic and Biological Colloids, Ministry of Education, School of Chemical and Material Engineering, Jiangnan University, Wuxi 214122, China*
[2] *Department of Radiation Oncology, Affiliated Hospital of Jiangnan University, Wuxi 214122, China*
[3] *Wuxi School of Medicine, Jiangnan University, Wuxi 214122, China*
[4] *Second Dental Center, Peking University School and Hospital of Stomatology, Beijing 100101, China*
[§] *Huixin Zhang and Hao Hang contributed equally to this work.*

Cite this article: *Nano Research*, **2025**, *18*, 94907385. https://doi.org/10.26599/NR.2025.94907385

ABSTRACT: While a variety of wound dressing materials are available, the effective combination of multiple active components into a single composite dressing to optimize wound healing outcomes presents a substantial challenge. Herein, we introduce a novel trilayer nanofiber membrane (SNM) for accelerated infected wound healing. The SNM, fabricated via electrospinning, comprises a hydrophilic inner layer enriched with epigallocatechin-3-gallate (EGCG) for antioxidant activity, an antimicrobial middle layer incorporating silver zeolitic imidazolate framework (Ag-ZIF), and a hydrophobic outer layer of waterborne polyurethane (WPU) for structural integrity. The SNM exhibits superior mechanical properties, with a tensile strength of 8.83 ± 0.99 MPa and an elongation at break of 262.57% ± 30.06%, alongside a water vapor transmission rate (WVTR) of 521 g/(m²·24h). The SNM composites demonstrate potent bactericidal effects, achieving a 93.50% ± 5.77% and 94.39% ± 4.29% reduction against *E. coli* and *S. aureus*, respectively. Furthermore, the SNM exhibits a high 2,2-diphenyl-1-picrylhydrazyl (DPPH) free radical scavenging efficiency of 95% at a concentration of 100 μg/mL. Animal studies indicate significant wound healing enhancement, with the SNM-treated group achieving a 52.78% healing rate on day 3, compared to 11.15% for the control group. This work offers a promising strategy for the development of multifunctional wound dressings with integrated antibacterial nanomaterials and natural bioactive components within a single composite material.

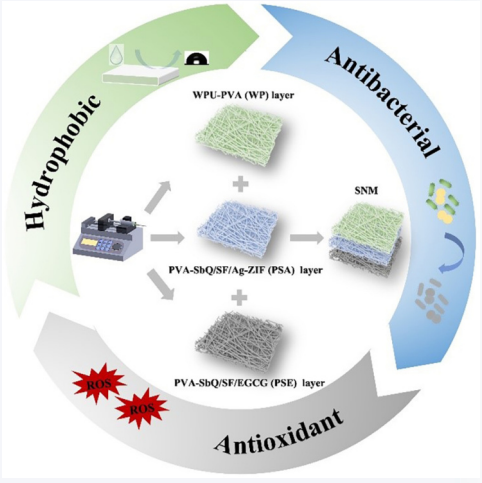

KEYWORDS: trilayer nanofiber membrane, integration, electrospinning, wound dressing, antibacterial property

1 Introduction

The integumentary system, primarily composed of the skin, fulfills crucial physiological roles such as protection, thermoregulation, and sensory perception [1, 2]. However, disruptions in the skin's barrier function, often caused by trauma, heighten susceptibility to microbial colonization and infection. Consequently, effective infection control strategies are crucial for achieving optimal wound healing [3]. Wound healing is a complex biological process influenced by various factors. An ideal wound dressing should possess a combination of properties, including antimicrobial activity, absorbency, moisture retention, and the capability to facilitate tissue regeneration [4, 5]. Two significant obstacles to wound healing are innate bacterial resistance and the excessive and prolonged production of reactive oxygen species (ROS) due to chronic inflammation. The indiscriminate use of antibiotics has led

Received: December 23, 2024; **Revised:** March 9, 2025
Accepted: March 18, 2025

✉Address correspondence to Han Zhu, zhysw@jiangnan.edu.cn; Mingliang Du, du@jiangnan.edu.cn; Chanyuan Jin, jinchanyuanjcy@163.com; Jianfeng Huang, 9862019007@jiangnan.edu.cn

to a global health crisis: antibiotic resistance. Bacteria have developed resistance mechanisms against a wide range of antibiotics, rendering infections more challenging and expensive to treat. While ROS plays a pivotal role in the early stages of wound healing, their excessive and persistent generation can induce oxidative stress, which damages tissues, inhibits cell proliferation, and delays the healing process [6, 7]. Chronic inflammation is often accompanied by elevated ROS levels, further impairing wound healing. Consequently, there is an urgent need to develop innovative wound dressings that can simultaneously address the dual challenges of antibiotic resistance and ROS regulation.

A promising strategy to combat the escalating issue of antibiotic resistance involves the development of innovative antibacterial nanomaterials [8]. These materials have the potential to mitigate the emergence of bacterial resistance, thereby enabling the effective treatment of infections without exclusive reliance on traditional antibiotics. Ag-based materials have garnered significant attention as potent antimicrobial agents due to their broad-spectrum activity and relatively low toxicity. When reduced to the nanoscale, Ag exhibits substantially enhanced antibacterial properties compared to its bulk counterpart. This enhancement is attributed to the increased surface area of nanoparticles (NPs), facilitating more efficient interaction with bacterial cells. However, excessive exposure to Ag can lead to adverse health consequences, including cardiovascular and dermatological issues [9, 10]. Therefore, it is imperative to address the challenges associated with size, concentration, and stability of Ag NPs, while maintaining their antimicrobial efficacy. Natural antioxidants, such as silk, a natural protein derived from silkworms and other organisms, primarily composed of silk fibroin (SF) and sericin, have been explored to neutralize excess ROS [11, 12]. By neutralizing ROS, silk can facilitate wound healing by stimulating cell proliferation, migration, and tissue regeneration [13]. However, the rich in electron-donating groups make them highly susceptible to oxidation when exposed to heat and light. Developing effective strategies to overcome this limitation and enhance their stability is highly desirable.

In the process of wound healing, dressings play a crucial role beyond providing a physical barrier. They are expected to exhibit multiple functions, including antibacterial activity, wound healing promotion, and moisture retention. The integration of antibacterial nanomaterials and natural bioactive components within a single composite material represents a promising strategy for the development of multifunctional wound dressings [14]. Electrospinning, a versatile fabrication technique, offers the potential to encapsulate these agents within a protective polymer nanofiber matrix [15, 16]. This approach enables the creation of multifunctional dressings that not only exhibit antimicrobial activity but also promote tissue regeneration, reduce inflammation, and enhance wound healing [17]. In addition, electrospinning enables the production of nanofiber membranes with high specific surface area, good breathability, and adjustable mechanical properties, representing a significant advantage [18]. These membranes can mimic the structure of natural cell matrices, providing favorable growth environments for cells, promoting cell adhesion and proliferation, and accelerating wound healing processes [19, 20]. Nevertheless, significant challenges persist in ensuring component compatibility, achieving controlled release of both antimicrobial and antioxidant agents, maintaining composite stability across diverse environmental conditions (e.g., pH, temperature, humidity), and realizing synergistic interactions between antimicrobial and antioxidant properties.

In this work, to address these limitations, we have designed a multifunctional sandwich-structured nanofiber membrane (SNM) for wound dressings. The polyvinyl alcohol-styrene-bipyridinium salt (PVA-SbQ) blended with SF serves as a biocompatible polymer matrix, while the encapsulated epigallocatechin gallate (EGCG) provides potent antioxidant properties. This PVA-SbQ/SF/EGCG composite functions as the inner layer (PVA-SbQ/SF/EGCG (PSE)), efficiently absorbing wound exudates and creating a biocompatible microenvironment conducive to wound healing. The intermediate layer (PVA-SbQ/SF/Ag-ZIF (PSA)) incorporates MOF-supported Ag NPs into the PVA-SbQ/SF nanofiber matrix, providing a robust antimicrobial barrier. The MOF stabilizes Ag ions and Ag NPs, ensuring the controlled release of Ag ions for enhanced sustained antimicrobial efficacy. The outer layer (WPU/PVA (WP)), composed of water-borne polyurethane-PVA (WPU-PVA) composite material, exhibits excellent hydrophobicity, effectively preventing external contaminants from adhering to the dressing. This layer serves as a physical barrier, protecting the active components in the inner layers from direct exposure to the external environment. Additionally, it enhances the mechanical strength of the dressing, reducing the risk of rupture or detachment during use. The SNM composites demonstrate potent bactericidal effects, achieving 93.50% ± 5.77% and 94.39% ± 4.29% reduction against *E. coli* and *S. aureus*, respectively. Furthermore, the SNM exhibits a high 2,2-diphenyl-1-picrylhydrazyl (DPPH) free radical scavenging efficiency of 95% at a concentration of 100 μg/mL. Animal studies indicate significant wound healing enhancement, with the SNM-treated group achieving a 52.78% healing rate on day 3, compared to 11.15% for the control group.

2 Results and discussion

Figure 1(a) depicts the electrospinning process employed to fabricate SNM. The SNM comprises three distinct layers, each contributing to its exceptional properties (Fig. 1(b)). The outer layer (WP) is a hydrophobic support layer composed of a binary blend of water-borne polyurethane (WPU) and PVA (Fig. 1(c)). The WP layer with excellent enhanced mechanical strength and thermal stability provides the supporting function and contributes to the overall mechanical properties of the whole SNM. Meanwhile, the hydrophobicity of WP provides a certain level of barrier against external bacteria and moisture. The intermediate layer (PSA) is an antibacterial layer incorporating the antibacterial agent Ag-ZIF within a matrix of PVA-SbQ and SF (Fig. 1(d)). The primary function of the PSA layer is to provide antibacterial activity. As is shown in Fig. 1(e), the inner layer (PSE) is a hydrophilic drug-loading layer composed of a ternary blend of PVA-SbQ, SF, and EGCG. The PSE layer, directly interfacing with the wound skin, exhibits favorable wettability, appropriate breathability, and significant antioxidant capacity.

The surface morphologies of ZIF-8 and Ag-ZIF were characterized in detail by field emission scanning electron microscopy (FE-SEM) and scanning transmission electron microscopy (STEM). Figures 2(a) and 2(b) illustrate the characteristic rhombic dodecahedral morphology of ZIF-8 nanoparticles (NPs), with an average size of approximately 72.44 ± 0.61 nm (Fig. S1(a) in the Electronic Supplementary Material (ESM)). Upon the incorporation of Ag into ZIF-8 NPs, a

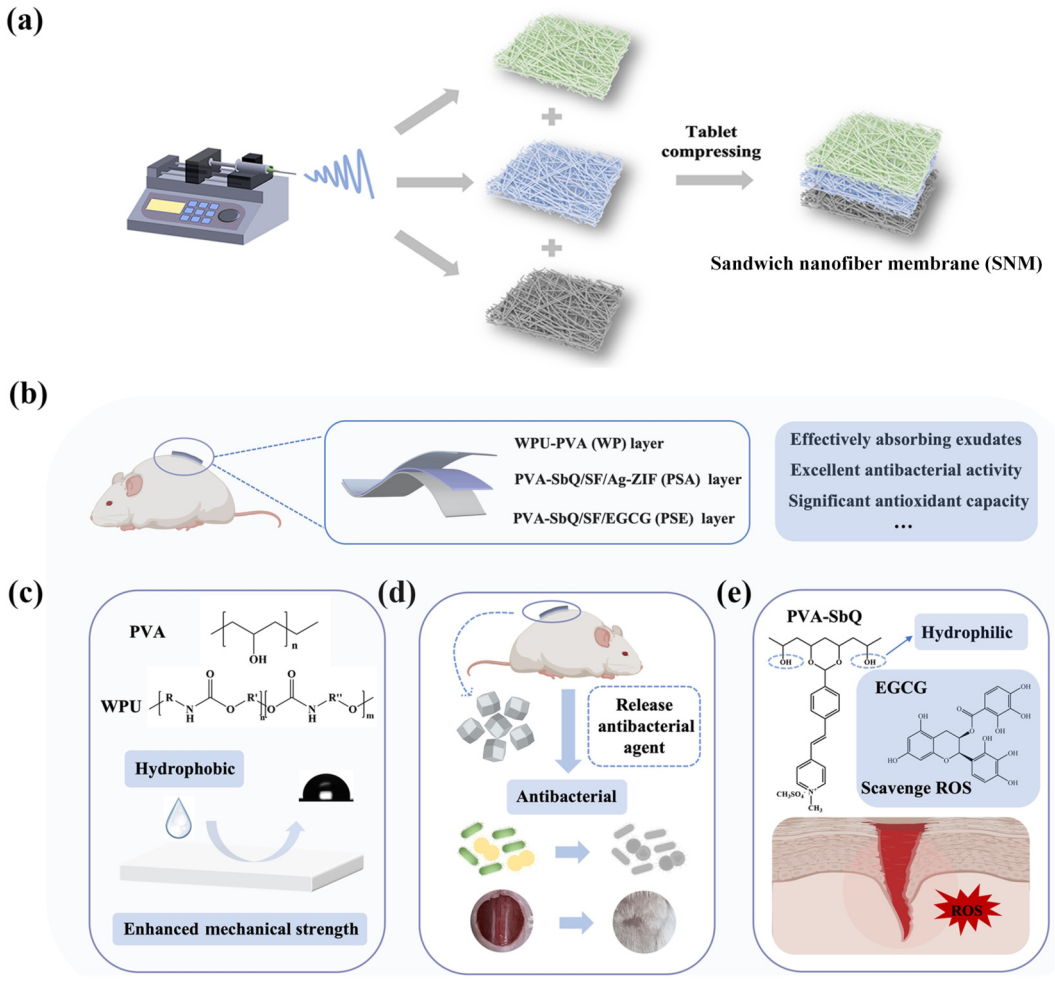

Figure 1 (a) Schematic illustration for the fabrication process of sandwich-structured nanofiber membranes via electrospinning. (b) Schematic representation of the sandwich-structured nanofiber membrane comprising the WP, PSA, and PSE layers. (c) The outer layer (WP) is a hydrophobic support layer composed of a WPU-PVA blend, providing a barrier against external bacteria and moisture. (d) The intermediate layer (PSA) is an antibacterial layer incorporating Ag-ZIF. This layer provides sustained release of Ag ions, which exhibit potent antimicrobial activity against a broad spectrum of bacteria. (e) The inner PSE layer, directly interfacing with the wound skin, exhibits favorable wettability, allowing for efficient exudate absorption and moisture exchange. Its significant antioxidant capacity helps to mitigate oxidative stress and promote tissue regeneration.

discernible morphological transition from the distinct rhombic dodecahedron to a more spherical morphology is observed (Figs. 2(c) and 2(d)). The average diameter of the resulting Ag-ZIF NPs is 70.29 ± 1.01 nm (Fig. S1(b) in the ESM), which is comparable to the average diameter of pristine ZIF-8 NPs. Additionally, the presence of Ag NPs with diameters less than 10 nm was observed on the surface of the Ag-ZIF NPs, suggesting a strong interfacial interaction between the Ag NPs and the ZIF-8 framework. High-resolution transmission electron microscopy (HRTEM) image indicates the well-defined lattice fringes (Fig. 2(e)), confirming the crystalline nature of the synthesized Ag NPs. The interplanar d-spacing, measured to be 2.3 Å, is in agreement with the (111) planes of face-centered cubic (FCC) Ag phase [21]. To gain deeper insights into the distribution of Ag within the Ag-ZIF composite, scanning transmission electron microscopy-energy dispersive X-ray spectroscopy (STEM-EDS) elemental mapping was conducted. Figure 2(f) clearly indicates the presence of Ag, either on the surface or within the pores of the ZIF-8 framework, thus providing strong evidence for the successful formation of Ag NPs.

As shown in Fig. 3(a), the Fourier transform infrared spectroscopy (FTIR) of ZIF-8 reveals characteristic vibrational bands consistent with the features of the 2-methylimidazole (H-MIM) organic ligand. Specifically, prominent bands observed at approximately 3135 and 2929 cm^{-1} can be attributed to the N–H and C–H stretching vibrations, respectively. The peak at 1585 cm^{-1} corresponds to the C–N stretching mode, while the strong and complex peaks centered at 1459, 1424, and 1309 cm^{-1} are associated with the stretching vibrations of the imidazole ring. The FTIR spectrum of ZIF-8 exhibits characteristic vibrational bands in the frequency range of 996–1309 cm^{-1} and below 800 cm^{-1}, which are attributed to the in-plane and out-of-plane bending vibrations of the imidazole rings, respectively. Notably, the sharp peak at 422 cm^{-1} is attributed to Zn–N stretching vibration, further confirming the formation of ZIF-8 framework [22–24]. A comparison of the FTIR spectra of ZIF-8 and Ag-ZIF reveals a high degree of similarity in the characteristic vibrational peaks, suggesting that the incorporation of Ag NPs does not significantly disrupt the underlying ZIF-8 structure.

Figure 3(b) presents the X-ray diffraction (XRD) patterns of ZIF-8 and Ag-ZIF. The diffraction peaks at 7.3°, 10.3°, 12.7°, 14.8°, 16.4°, 18.0°, 22.1°, 24.5°, 26.7°, and 29.7° correspond to the (011), (002),

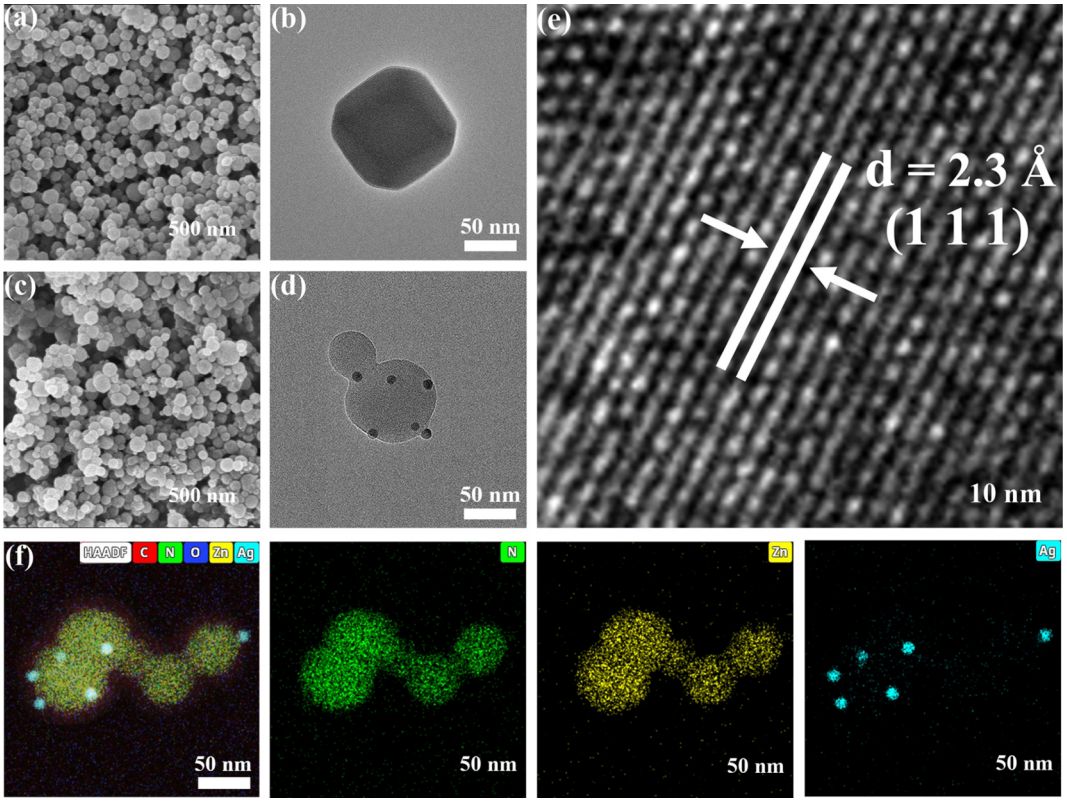

Figure 2 FE-SEM and TEM images of ((a) and (b)) ZIF-8 NPs and ((c) and (d)) Ag-ZIF NPs. (e) HRTEM image of Ag NPs in Ag-ZIF. (f) STEM-EDS elemental mapping images of Ag-ZIF NPs.

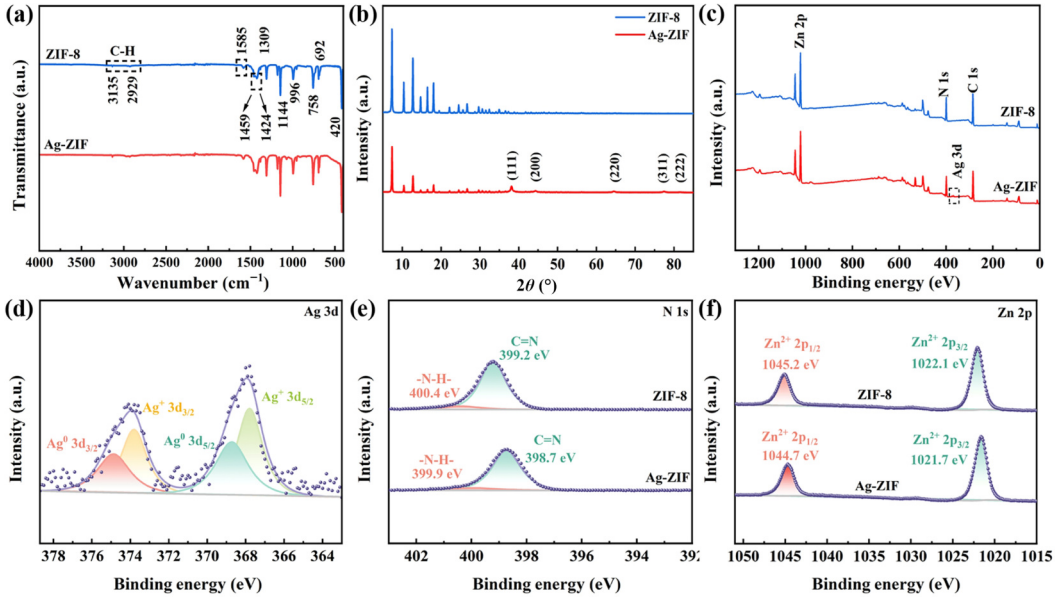

Figure 3 (a) FTIR spectra, (b) XRD patterns, and (c) XPS survey spectra of ZIF-8 NPs and Ag-ZIF NPs. (d) Ag 3d XPS spectra of Ag-ZIF NPs. (e) N 1s and (f) Zn 2p spectra of ZIF-8 NPs and Ag-ZIF NPs.

(112), (022), (013), (222), (114), (233), (134), and (044) crystal planes of ZIF-8, respectively, verifying the successful synthesis of phase-pure ZIF-8 [25]. The XRD pattern of Ag-ZIF shows similar diffraction peaks to that of pristine ZIF-8, with no significant shifts in peak positions, suggesting that the growth of Ag has minimal impact on the underlying ZIF crystal structures. However, the observed decrease in peak intensities for Ag-ZIF indicates that the growth of Ag NPs may partially occlude the surface of the ZIF-8 crystal. The XRD pattern of Ag-ZIF revealed peaks at 2θ = 38.1°, 44.3° 64.5°, 77.5° and 81.6°, indexed to the (111), (200), (220), (311) and (222) planes of metallic Ag, respectively (JCPDS no. 04–0783), confirming the successful synthesis of the Ag-ZIF [26]. The Ag content was determined to be 2.08%, as evidenced by inductively coupled plasma optical emission spectrometry (ICP-OES, Table S1 in the ESM).

X-ray photoelectron spectroscopy (XPS) was employed to

investigate the surface chemical composition and binding states of the samples. The binding energies were referenced to the C 1s peak at 284.8 eV. XPS survey spectra (Fig. 3(c)) reveals the presence of C, N and Zn elements in all samples. The emergence of XPS peaks attributed to the Ag in Ag-ZIF sample provides strong evidence for the successful incorporation of Ag NPs into the ZIF-8 framework. As shown in Fig. 3(d), the high-resolution Ag 3d XPS spectra of Ag-ZIF exhibit two main peaks at 368.0 and 374.0 eV, separated by 6.0 eV, corresponding to the Ag $3d_{5/2}$ and Ag $3d_{3/2}$ orbitals, respectively [27]. Further deconvolution of these peaks reveals two distinct pairs of peaks. The lower-energy pair at 368.7 and 374.9 eV is attributed to the metallic Ag^0 species, while the higher-energy pair at 367.8 and 373.8 eV corresponds to Ag^+ species [21]. As shown in Table S2 in the ESM, the relative abundance of Ag^+ and Ag^0 species in Ag-ZIF is estimated to be 56.53% and 43.47%, respectively. This observation reveals that Ag ions (Ag^+) coexist with Ag NPs in Ag-ZIF, with a portion of the surface-bound Ag species underwent reduction to form Ag NPs, while the remaining Ag^+ species remained coordinated with H-MIN ligand. In the N 1s spectrum of ZIF-8 (Fig. 3(e)), two peaks were observed at 400.4 and 399.2 eV, corresponding to the –NH– and C=N bonding, respectively [28]. Upon Ag NPs loading, the peaks shifted to 399.9 and 398.7 eV, respectively, indicating a change in the electronic environment of the nitrogen atoms. In the Zn 2p spectra of ZIF-8 (Fig. 3(f)), the binding energies (BEs) of Zn $2p_{1/2}$ and Zn $2p_{3/2}$ were determined to be 1045.2 and 1022.1 eV, respectively [29]. This indicates the presence of Zn in a bivalent state within the ZIF-8. In the Zn 2p spectra of Ag-ZIF, the two peaks at 1044.7 and 1021.7 eV were assigned to Zn^{2+} $2p_{1/2}$ and Zn^{2+} $2p_{3/2}$, respectively. A slight decrease in BEs of Zn in Ag-ZIF suggests a potential electronic interaction between Ag and Zn species. These results provide strong evidence for the successful incorporation of Ag species within the ZIF-8 framework, likely involving the substitution of Zn^{2+} ions by Ag^+ ions and the formation of Ag–N coordination bonds with the H-MIM ligands.

The layered structure of the SNM, comprising WP, PSA, and PSE layers, is visualized in the digital micrograph shown in Figs. 4(a) and 4(b). As shown in Fig. 4(c), the cross-sectional FE-SEM image of the SNM exhibits well-defined interfaces and strong interfacial adhesion between the individual WP, PSA, and PSE layers. The thicknesses of these layers were determined to be 9.52, 18.09, and 20.59 μm, respectively. A hydrophobic support layer (WP), composed of WPU and PVA, is integrated as the outermost layer. This layer enhances water resistance, provides mechanical support, and contributes to the overall mechanical integrity of the SNM. Figures 4(d) and 4(g) indicate the smooth surfaces of the WPU/PVA nanofibers, with an average diameter of 230.7 ± 4.3 nm (Fig. S2(a) in the ESM). The intermediate layer, designated as the PSA layer, incorporates antibacterial Ag-ZIF within a matrix of PVA-SbQ and SF to provide antibacterial properties (Figs. 4(e) and 4(h)). The PSE layer with an average diameter of 206.9 ± 3.5 nm exhibits well-dispersed Ag-ZIF in nanofibers (Fig. S2(b) in the ESM). The inner layer of the SNM, composed of PVA-SbQ, SF, and EGCG, is denoted as the PSE. The PSE layer exhibits a disordered and randomly distributed interwoven nanofiber morphology, with an average diameter of approximately 266.8 ± 4.0 nm (Figs. 4(f) and

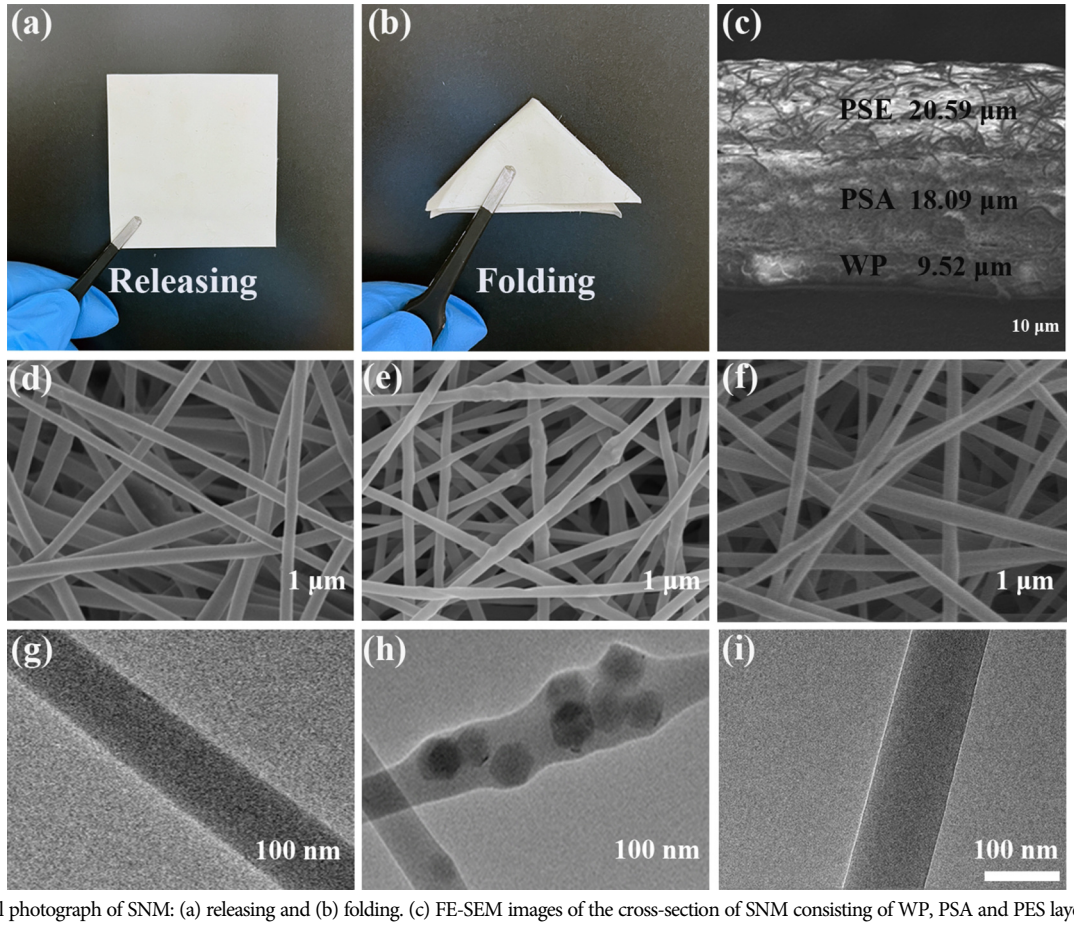

Figure 4 Digital photograph of SNM: (a) releasing and (b) folding. (c) FE-SEM images of the cross-section of SNM consisting of WP, PSA and PES layers. FE-SEM and TEM images of ((d) and (g)) WP, ((e) and (h)) PSA, and ((f) and (i)) PSE layers.

4(i), and Fig. S2(c) in the ESM).

FTIR spectra and XRD patterns were employed to characterize the chemical and crystal structures of the individual nanofiber membrane layers and the SNM composites. As shown in Fig. 5(a), the FTIR spectrum of WP layers exhibits a broad absorption band centered at approximately 3358 cm^{-1}, corresponding to the N–H stretching vibration of WPU. Additionally, a series of absorption peaks in the 3000–2800 cm^{-1} region are observed, attributed to C–H stretching vibrations. The strong absorption peak at 1728 cm^{-1} corresponds to the stretching vibration of the carbonyl (–C=O) group, indicating the presence of ester and amide groups in both PVA and WPU [30]. Furthermore, the absorption peak at 1128 cm^{-1} reveals the C–O–C stretching vibration, which is associated with ether groups in WPU. For both PSA layers and PSE layers, prominent –OH stretching peaks are observed at 3285 cm^{-1}. A characteristic absorption peak at 1246 cm^{-1} is present, corresponding to the C–O stretching vibration, suggesting the presence of PVA [31]. Notably, the intensity of the –OH absorption peak in PSA layers is significantly higher than that observed in PSE layers. This difference may be attributed to the strong hydrogen between the catechol groups in EGCG molecules within PSE layers and the functional groups of PVA-SbQ and SF within PSA, leading to enhanced intermolecular interactions. The FTIR spectrum of the SNM composite displays all the characteristic peaks observed in the individual components, confirming the successful material integration. As shown in Fig. S3 in the ESM, XRD patterns reveal that the WP layers and PSE layers display amorphous characteristics, with a prominent carbon peak at 2θ = 20°. Conversely, Ag-ZIF retains its crystalline nature, as evidenced by the persistence of three diffraction peaks (011), (002), and (112) in the PSA layers. The SNM composite material, fabricated via physical compression, exhibits typical amorphous properties. These results further confirm the successful preparation of WP/PSE/PSA sandwich membrane.

Mechanical performance is paramount in wound dressing design, influencing stability, safety, and wound healing. Ideally, wound dressings should possess a tensile strength of 1–32 MPa and an elongation at break exceeding 40% [32, 33]. As shown in Fig. 5(b), the SNM composite material demonstrates superior mechanical properties, with a tensile strength of 8.83 ± 0.99 MPa and an elongation at break of 262.57% ± 30.06%. Interestingly, the incorporation of Ag-ZIF NPs significantly enhances the tensile strength of PSA layer (5.37 ± 0.74 MPa) compared to PSE layer (2.61 ± 0.32 MPa). These Ag-ZIF NPs, characterized by their small size and high specific surface area, form robust interfacial bonds with the nanofiber matrix, impeding crack propagation [34]. Conversely, the weaker hydrogen bonding between EGCG and the matrix in PSE layer results in lower tensile strength. However, the PSE layer exhibits higher elongation at break, likely due to the enhanced flexibility from hydrogen bonding between EGCG and PVA-SbQ molecular chains, which effectively dissipates energy during stretching and delay fracture [35]. As shown in Fig. S4 in the ESM, the SNM composite material exhibits a stepped stress-strain curve, indicative of its complex composite structure and component interactions. Initially, the combined WP, PSA, and PSE layers resist external forces. As strain increases, the individual components (e.g., PSA and PSE) begin to fail, leading to stress drops. Subsequently, other components continue to resist deformation causing stress to rise again, resulting in a stepped curve. At approximately 250% strain, all components approach fail, resulting in material fracture. This stepped stress-strain behavior highlights the intricate mechanical response and synergistic interaction of the various components within SNM composite materials during tensile deformation.

The thermal stability of the individual layers and SNM composite was investigated using thermogravimetric analysis (TGA) and differential thermal gravimetry (DTG) (Fig. 5(c) and Fig. S5 in the ESM). As shown in Fig. 5(c), the WP layer undergoes complete degradation at 500 °C, resulting in a 100% weight loss. In contrast, the PS-based materials exhibit a three-stage thermal degradation profile. The initial stage, occurring between 80–130 °C, is attributed to the desorption of adsorbed water molecules from the nanofiber membrane, leading to a mass loss of approximately 5% [36]. The second stage, spanning 230–350 °C, is characterized by significant degradation. As the temperature increases, the cleavage of chemical bonds within the polymer chains is initiated, leading to the release of volatile small molecules. In the final stage, from 350–500 °C , the removal of hydroxyl groups from the

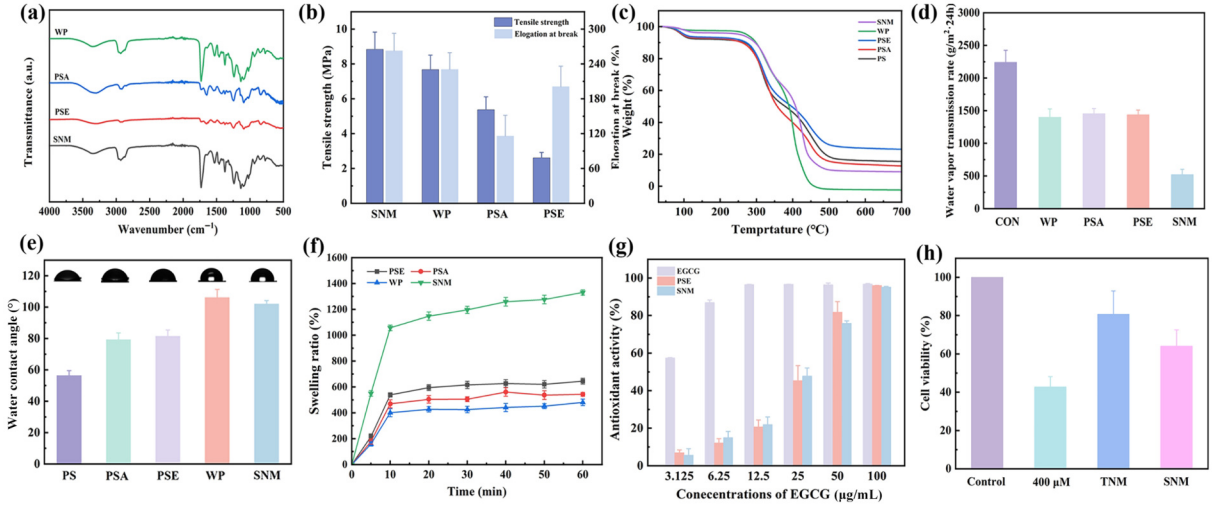

Figure 5 (a) FTIR spectra, (b) mechanical properties, and (c) TG curves of the WP layer, PSA layer, PSE layer, and the SNM composites. (d) Water vapor transmission rate of the control, WP layer, PSA layer, PSE layer, and the SNM. (e) Water contact angles of the PS, PSA layer, PSE layer, WP layer, and SNM. (f) Swelling curves of the WP layer, PSA layer, PSE layer, and the SNM composites. (g) Antioxidant activity evaluation of free EGCG, PSE, and SNM evaluated by the DPPH· radical scavenging efficiency. (h) *In vitro* antioxidant capacity of different materials evaluated by L929 cell viability under 400 μM H_2O_2-induced oxidative damage.

polymer backbone takes place, resulting in the formation of gaseous and solid residues, including carbon and zinc oxide (ZnO) [37]. As shown in Fig. S5 in the ESM, the incorporation of EGCG and Ag-ZIF into PS nanofibers significantly reduces the rate of degradation during the second stage (230–350 °C) and shifts the degradation temperature to a higher range (250–390 °C), suggesting an enhancement in the thermal stability of the composite nanofibers.

Water vapor transmission rate (WVTR) is a critical parameter for evaluating the performance of wound dressings during wound healing. Ideally, the WVTR for wound dressings typically ranges from 76 to 9360 g/(m^2·24h) [38]. In order to accurately evaluate the moisture permeability of individual layers and SNM composite, unsealed centrifuge tubes were designated as the control group (CON). Centrifuge tubes sealed with WP layer, PSA layer, PSE layer, and SNM composite were designated as the experimental groups. As shown in Fig. 5(d), the CON group exhibited a WVTR of 2242 g/(m^2·24h), while the WP layer, PSA layer, and PSE layer demonstrated the WVTR values of 1400, 1453, and 1438 g/(m^2·24h), respectively. Notably, the SNM composite composed of WP, PSA, and PSE layers significantly reduced the WVTR to approximately 521 g/(m^2·24h), which is approximately one-third of the aforementioned individual layers. Compared to the control group, all of the WP layer, PSA layer, and PSE layer exhibited lower WVTR due to the inherent barrier properties of the nanofiber structure. However, as the pore size of individual layers significantly exceeds the molecular diameter of water vapor (0.0004 μm), water vapor can still permeate through these pores [39]. The results indicate that the prepared SNM possesses suitable water vapor permeability, facilitating gas exchange and preventing the accumulation of wound exudate, thereby promoting optimal wound healing.

The surface wettability of individual layers and SNM was evaluated through water contact angle (WCA) analysis. As illustrated in Fig. 5(e), the WP layer exhibited the poorest wettability, with a WCA of up to 106.25°, indicating strong hydrophobic properties. This makes WP a suitable candidate for the outer layer of wound dressings, providing effective resistance to external moisture and bacterial penetration. In contrast, the PS substrate demonstrated good hydrophilicity, with a contact angle of 56.45°. To investigate the effect of Ag-ZIF on the surface wettability of the nanofiber membranes, PVA-SbQ/SF nanofiber membranes without Ag-ZIF, denoted as PS, were prepared as a control. The PS membrane shows the lower WCA of 56.45° while the PSA layer containing Ag-ZIF achieves the WCA of 79.32°. This enhanced hydrophobicity can be attributed to the introduction of Ag-ZIF NPs, which modifies the surface morphology and roughness of the nanofiber membrane, thereby influencing the interaction between the membrane surface and water molecules [40, 41]. Furthermore, the incorporation of EGCG increased the WCA of PSE layer to 81.57°, indicating a shift towards hydrophobicity. This transformation is likely due to intermolecular π-π stacking and hydrogen bonding interactions among the catechol groups in EGCG, PVA-SbQ, and SF [42]. However, the WCA of PSE layer remains below 90°, indicating that the material retains suitable hydrophilicity for the rapid absorption of wound exudate. Consequently, PSE is well-suited for direct contact with the skin as the inner layer of a wound dressing.

Swelling behavior, a key property of wound dressings, is crucial for effective exudate management. A high swelling capacity facilitates the absorption of wound exudate, thereby maintaining a clean microenvironment and preventing infection. The swelling behavior of different fibrous membrane materials, including PSE, PSA, WP, and SNM, was investigated by measuring their mass changes at designated time intervals over 60 min following water absorption. As illustrated in Fig. 5(f), all the samples exhibited high liquid absorption, attaining swelling equilibrium within approximately 10 min. Notably, the SNM, with its tri-layer structure, demonstrated the highest swelling capacity, absorbing up to 13 times its initial mass after 60 min, indicating its exceptional liquid absorption. Swelling capacity is primarily governed by the concentration of hydrophilic functional groups and the internal porous architecture of the material. Conversely, WP displayed the lowest swelling performance, attributed to its composition of water-based WPU.

The antioxidant properties of the individual layers and SNM composite are primarily attributed to the presence EGCG, a bioactive compound renowned for its significant role in promoting wound healing. As shown in Fig. 5(g), the free EGCG exhibits a concentration-dependent radical scavenging capacity. Increasing EGCG concentration correlates with enhanced radical scavenging ability, reaching over 95% efficiency at a concentration of 12.5 μg/mL. Notably, both the PSE layer and SNM composite exhibit comparable radical scavenging abilities to free EGCG at this concentration, suggesting that the compression process does not compromise EGCG's biochemical activity. However, the PSE layer and SNM composite exhibit significantly lower radical scavenging efficiency compared to the EGCG solution. This reduction can be attributed to two primary factors. EGCG's numerous hydroxyl groups facilitate intermolecular hydrogen bonding with hydroxyl groups in PVA-SbQ and carboxyl and hydroxyl groups in SF, leading to its entrapment within the nanofiber matrix. On the other hand, the encapsulation of EGCG within the nanofibers limits direct contact with the DPPH solution. Despite these limitations, increasing the EGCG concentration in PSE and SNM to 100 μg/mL enables them to achieve 95% efficiency in scavenging ROS. This property contributes to mitigating inflammatory responses and accelerating wound healing.

The ability of the SNM fibrous membrane to effectively scavenge ROS in a DPPH solution was established through prior free radical scavenging experiments. Subsequently, the antioxidant capabilities of SNM were corroborated via cellular assays. The cytoprotective properties of TNM and SNM materials were determined by assessing L929 cell viability in a high-concentration H_2O_2-induced oxidative stress environment, thereby providing a measurement of their antioxidant efficacy. The results exhibited that treatment of L929 cells with 400 μM H_2O_2 resulted in a significant reduction in cell viability to 42.8% (Fig. 5(h)). However, a significant enhancement in cell viability was observed when cells were co-cultured with TNM and SNM fibrous membranes containing EGCG, resulting in cell survival rates of 80.7% and 64.1%, respectively. These results underscore the strong antioxidant capabilities of the EGCG-incorporated fibrous membranes, effectively safeguarding cells against oxidative damage induced by high concentrations of H_2O_2. Notably, the SNM group demonstrated a lower viability than that of the TNM group. This phenomenon is attributed to the antibacterial layer (PSA) in the SNM, which contains the antibacterial agent Ag-ZIF. The Ag ions are known to be toxic to cell partially, which result in a slight decrease in cell viability detected in the SNM group.

The antibacterial efficacy of TNM (WP/PSE) bilayer and SNM

(WP/PSA/PSE) trilayer against *E. coli* and *S. aureus* was systematically evaluated using the standard disk agar diffusion method. A blank control and a kanamycin-treated positive control were included for comparison. As shown in Fig. 6(a), the TNM bilayer exhibited negligible antibacterial activity, as evidenced by the absence of a visible inhibition zone. Conversely, the SNM composite demonstrated substantial antibacterial effects, with inhibition zone diameters of 11.73 ± 0.25 and 10.70 ± 0.26 mm against *E. coli* and *S. aureus*, respectively (Figs. 6(c) and 6(d)). Statistical analysis confirmed a significant difference (***$P \le 0.001$) in antibacterial efficacy between SNM and TNM, highlighting the crucial role of the Ag-ZIF in PSA layer in enhancing antibacterial performance. While SNM exhibited promising antibacterial properties, its efficacy was lower than that of the kanamycin-treated positive control, which displayed inhibition zone diameters of 13.97 ± 0.15 and 13.80 ± 0.29 mm against *E. coli* and *S. aureus*, respectively. This discrepancy may be attributed to the limited amount of Ag present in the SNM wafer.

To further evaluate the antibacterial potency, co-culture experiments with *E. coli* and *S. aureus* were conducted using the plate spreading method (Fig. 6(b)). TNM exhibited moderate antibacterial activity, with inhibition rate of 27.84% ± 7.00% and 4.15% ± 5.78% against *E. coli* and *S. aureus*, respectively. In contrast, SNM demonstrated significantly higher antibacterial activity, with inhibition rates of 93.50% ± 5.77% and 94.39% ± 4.29% against *E. coli* and *S. aureus*, respectively (Figs. 6(e) and 6(f)). In comparison, the positive control group showed inhibition rates of 88.11% ± 2.66% against *E. coli* and 80.83% ± 3.68% against *S. aureus*, both of which were lower than those of SNM. The superior antibacterial performance of SNM can be attributed to multiple mechanisms. In SNM composite, the synergistic interaction between Ag NPs and Ag ions (Ag^+) significantly enhances their antibacterial efficacy. Ag NPs disrupt bacterial cell membranes by forming pores or altering membrane permeability, resulting in the leakage of intracellular contents and a rapid decline in bacterial activity [27]. Additionally, Ag NPs can induce oxidative stress by generating ROS, which damage bacterial DNA and proteins, impairing their physiological functions and inhibiting bacterial growth and reproduction [43]. Furthermore, Ag NPs act as a reservoir for Ag^+, steadily releasing Ag ions and thereby prolonging the antibacterial effect [44–46]. Once the cell membrane is compromised by Ag NPs, Ag^+ can penetrate the bacterial interior more easily, where they interact with critical biomolecules such as proteins and nucleic acids, leading to bacterial cell death. This interaction disrupts protein synthesis and interferes with nucleic acid replication and transcription, ultimately leading to the inhibition of bacterial growth and division, and subsequently, cell death [47–49]. The antibacterial mechanisms of Ag NPs and Ag^+ are synergistic: Ag NPs disrupt the cell membrane, facilitating the entry of Ag^+, which then interacts with intracellular biomolecules such as proteins and nucleic acids, further impairing bacterial function.

A cell counting kit-8 (CCK-8) assay was employed to systematically assess the cytotoxicity of WP layer, PSA layer, PSE

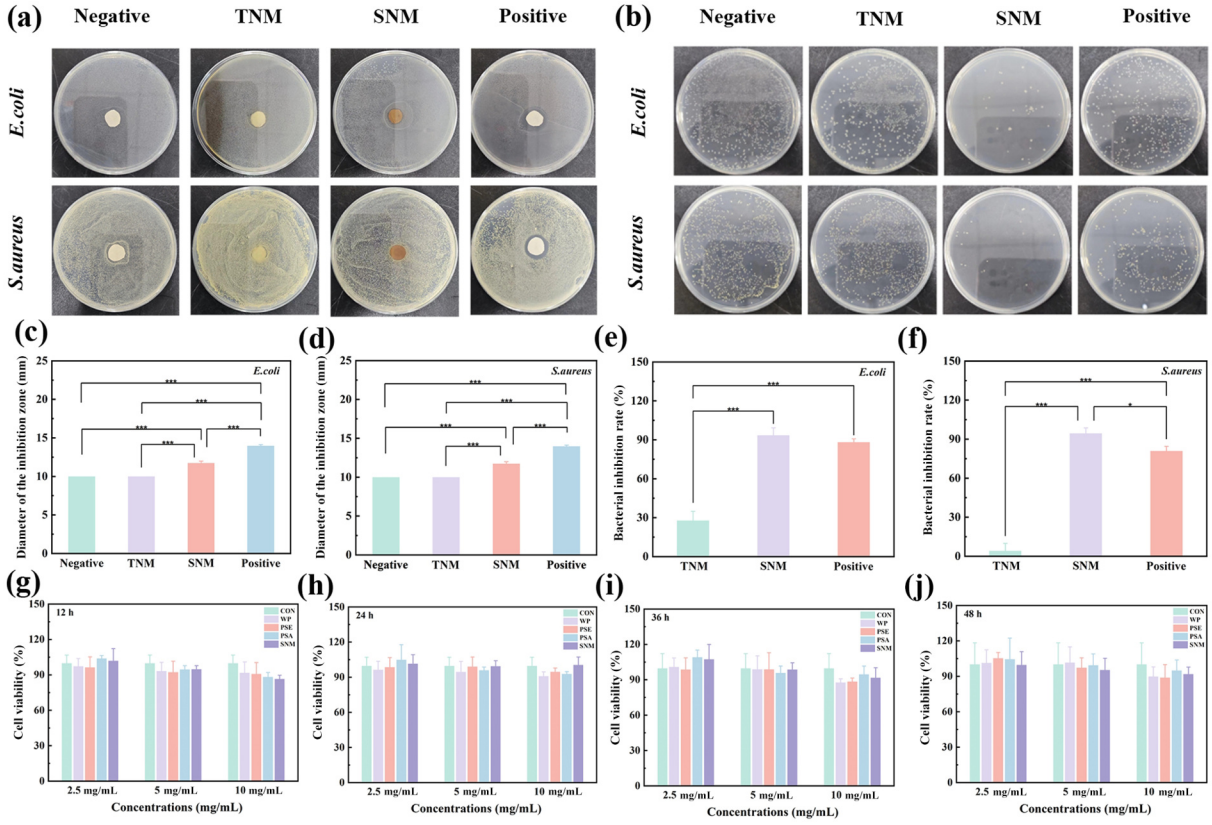

Figure 6 (a) Photographs depicting bacterial inhibition zones for various samples. (b) Photographs documenting LB agar plates inoculated with bacterial cultures and exposed to various samples' extraction solution, quantifying bacterial inhibition rates. The corresponding measured inhibition zone diameters on various samples against (c) *E. coli* and (d) *S. aureus*. The bacterial inhibition rates obtained on various samples against (e) *E. coli* and (f) *S. aureus*. The viability of L929 cells was assessed after exposure to various concentrations of various samples for durations of (g) 12, (h) 24, (i) 36, and (j) 48 h. Results are presented as mean ± standard deviation (n = 3). Statistical significance was determined by Student's t-test: *$P \le 0.05$, **$P \le 0.01$, ***$P \le 0.001$.

layer, and SNM composite on L929 cells. An untreated control group was included as a reference. The control group exhibited approximately 100% cell viability throughout the 48-h incubation period (12, 24, 36, and 48 h), indicating healthy cell growth. As shown in Figs. 6(g)–6(j) and Fig. S6 in the ESM, the L929 cells cultured with WP layer, PSA layer, PSE layer, and SNM composite at concentrations of 2.5, 5, and 10 mg/mL displayed increasing cell viability over time. A slight initial decrease in cell viability (0 h) was observed, likely due to the adaptation of cells to the new environment. However, from 12 h onwards, the cells proliferation accelerated, and viability significantly increased. At concentrations of 2.5 and 5 mg/mL, the cell viability consistently remained above 95%, suggesting the excellent biocompatibility of WP layer, PSA layer, PSE layer, and SNM composite with L929 cells. At a concentration of 10 mg/mL, a slight decrease in cell viability to approximately 90% was observed, suggesting a minor cytotoxicity.

According to the ISO 10993-5 standard, cell viability above 80% is considered as non-cytotoxic [50]. In this work, cell viability generally exceeded 90%, indicating that the experimental conditions, including the biomaterials and culture medium, were not significantly cytotoxic to L929 cells. The results suggest that the biomaterials demonstrated good biocompatibility with L929 cells at concentrations up to 5 mg/mL, supporting their potential applications in wound dressings. The *in vivo* bacteria-infected wound healing property of the various samples was evaluated using an *S. aureus*-infected mouse model on full-thickness skin wounds. Nanofiber membranes were administered topically to the infected wounds every three days for a total of 18 days post-infection. A control group (CON) with no treatment and a group treated with a commercially available dressing (SSD) served as comparators. The experimental results demonstrated that the SNM composite incorporating EGCG and Ag-ZIF exhibited the most effective wound healing properties among all experimental groups. Notably, SNM-treated wounds achieved complete closure by day 18 (Fig. 7(a)), consistent with the previous *in vitro* antibacterial assays. A detailed analysis of the wound area (Fig. 7(b)) and relative healing rate (Fig. 7(c)) confirmed the superior performance of the SNM dressing over the control group, likely due to its sustained release of Ag^+ and EGCG.

Notably, on the third day, the SNM group exhibited a significantly higher healing rate of 52.78%, compared to the control group's 11.15% (*$P \leq 0.001$), highlighting the superior efficacy of the SNM dressing. Moreover, the wound images (Fig. 7(a)) revealed potential complications associated with SSD dressing changes. The strong adhesion of SSD dressings may cause secondary wound trauma during replacement, particularly before scab formation, hindering efficient wound healing. In contrast, the TNM group, enriched with EGCG, demonstrated comparable wound healing to the SSD group during the initial six days (Fig. 7(b) and 7(c)), likely due to the release of EGCG, which is known to reduce inflammatory responses and oxidative stress.

During the early stages of wound healing, the SNM group exhibited significantly superior results compared to other groups, attributed to its multifaceted antibacterial, anti-inflammatory, and antioxidant capabilities. However, once the wound had scabbed over, the differences in efficacy between treatment groups became less pronounced. In conclusion, SNM dressings have demonstrated significant potential for accelerating the healing of infected wounds, particularly in the early stages, due to their multifunctional nature. These findings provide a strong scientific basis for the development of innovative and effective wound care materials.

As depicted in Figs. 7(d) and 7(e), the cumulative release curve of Ag ions from SNM exhibited distinct kinetic stage. During the initial 6 h, a rapid release of Ag ions was observed, reaching a cumulative release of 40.08%. Subsequently, the release rate gradually stabilized between 6 and 24 h, with cumulative release values of 43.87% at 12 h and 46.56% at 24 h. This biphasic release pattern suggests a sustained and controlled release of Ag ions from the fibrous membrane, facilitating prolonged antibacterial activity of SNM.

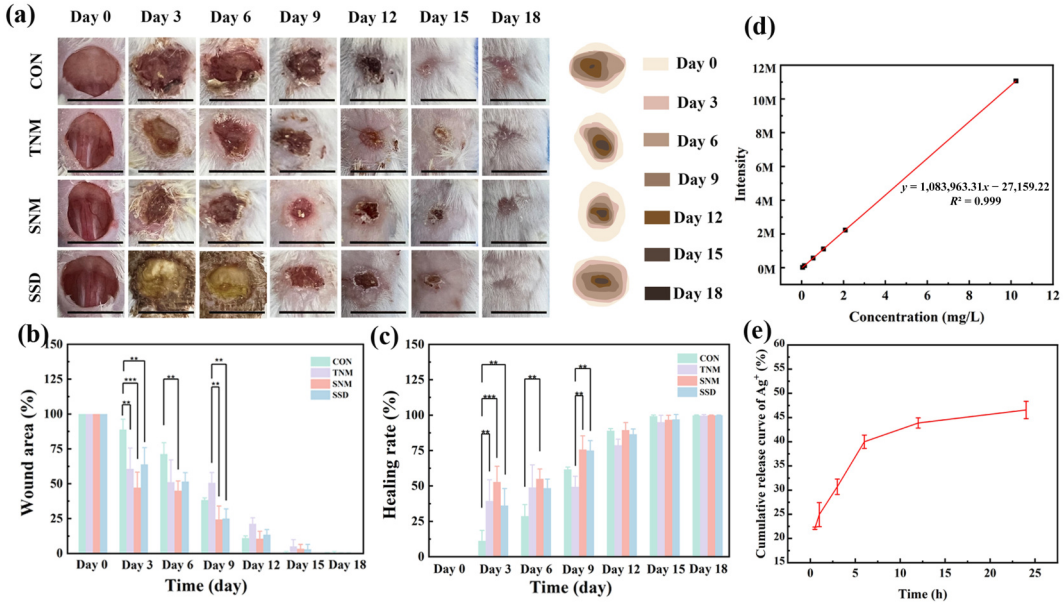

Figure 7 *In vivo* evaluation of various samples for wound healing. (a) Representative digital photographs of the wounds after 0, 3, 6, 9, 12, 15, and 18 days post-treatment. Scale bars = 10 mm. (b) Wound area, and (c) healing rate measured according to the images in (a). Results are presented as mean ± standard deviation ($n = 3$). Statistical significance was determined by Student's t-test: *$P \leq 0.05$, **$P \leq 0.01$, ***$P \leq 0.001$. (d) A silver nitrate standard curve prepared with concentration gradients of 0, 0.1, 0.5, 1.0, 2.0, and 10.0 mg/L, using 2% HNO_3 as the diluent. (e) Time-dependent cumulative release profile of Ag^+ from SNM materials.

The release of Ag ions from the substrate typically involves two key steps. Initially, the water molecules permeate the nanofiber network, inducing fibers swelling. Subsequently, driven by the concentration gradient, the ions diffuse from the substrate into the surrounding medium. Previous studies have demonstrated that the nanofibers, with high specific surface area and interconnected porous architecture, facilitate efficient ion diffusion pathways. In the initial stage of release, a significant concentration differential exists between the Ag ions encapsulated within the fibers and those in the surrounding medium, thereby driving the efflux of Ag ions. To gain a deeper understanding of the Ag ion release kinetics, the Higuchi model was utilized to fit the experimental data. The results showed that the model is highly consistent with the experimental data, with a correlation coefficient R^2 = 0.906, suggesting that the Ag ion release mechanism is primarily diffusion-controlled.

The animal wound healing studies revealed that the SNM dressing facilitated a wound healing rate of 52.78% in mice by day 3. This remarkable therapeutic effect is attributed to the synergistic antioxidant and antibacterial actions of the SNM dressing. To further investigate the bacterial colonization of wounds, Gram staining was performed on day 0 and 3 (Fig. 8). In this study, the mouse wounds were infected with *Staphylococcus aureus*. Here, it should be particularly clarified that for both time points, we collected wound exudate using a cotton swab, instead of directly excising mouse tissue, for Gram staining. Initial Gram staining on day 0 revealed the presence of *Staphylococcus aureus* across all treatment cohorts. After 3 days of therapeutic intervention with the designated dressings, a substantial decrease in Gram-positive bacterial populations was noted in all groups. Notably, the SNM-treated group displayed the most significant reduction in Gram-positive bacteria, thus underscoring the potent antibacterial properties of the SNM dressing. In contrast, the SSD and TNM treated groups demonstrated analogous outcomes. This observation is explained by the incorporation of EGCG within the TNM formulation, which imparts antibacterial activity, leading to a substantial reduction in Gram-positive bacteria relative to the untreated control. These experimental data corroborate the animal wound healing studies, reinforcing the potent antibacterial characteristics of the SNM material.

Cutaneous wound healing progresses through distinct phases, including hemostasis, inflammation, and granulation tissue formation. To evaluate treatment efficacy, histological analysis of wound site tissues was performed at 15 days post-treatment. Hematoxylin and eosin (H&E) staining was utilized to assess tissue regeneration. As shown in Fig. 8(b), In the Control and TNM groups, prominent neutrophil infiltration, characterized by numerous dark purple nuclear aggregations, was observed, along with localized tissue edema, loose stroma, and widened fiber gaps. The epidermis and dermis displayed relatively disordered structures, including defects in the TNM group, accompanied by significant capillary congestion and discernible hemorrhagic spots. Conversely, the SNM and SSD groups exhibited reduced neutrophil infiltration and attenuated edema, with relatively dense and organized stroma.

They showed intact epidermal continuity, nearly normal structure, and an absence of observable hemorrhage. These findings provide robust evidence for effective wound healing at the microscopic level, further substantiating the differential effects of the various treatments on the healing process. The antibacterial and antioxidant properties of SNM were further supported by histological analysis (H&E staining), which demonstrated its efficacy in promoting wound healing.

3 Conclusions

In summary, we developed a novel SNM nanocomposites incorporating Ag-ZIF and EGCG for effective infected wound management. Ag-ZIF exhibited strong antibacterial activity with low cytotoxicity, making it a promising antimicrobial agent. The SNM is constructed from a blend of PVA-SbQ/SF, with PVA-SbQ providing crosslinking under ultraviolet light, thereby enhancing the membrane's stability and mechanical properties. The hydrophilic inner layer is enriched with EGCG, while the antimicrobial middle layer incorporates Ag-ZIF, and the hydrophobic outer layer, composed of WPU, ensures structural integrity. The SNM demonstrated excellent mechanical strength, thermal stability, water vapor permeability, and biocompatibility. Antibacterial assays confirmed its broad-spectrum efficacy against *E. coli* and *S. aureus*. Furthermore, *in vivo* wound healing studies demonstrated accelerated wound healing in an *S. aureus*-infected model, highlighting the SNM's potential as a promising and versatile wound dressing material due to its combined antimicrobial, antioxidant, and biocompatible properties.

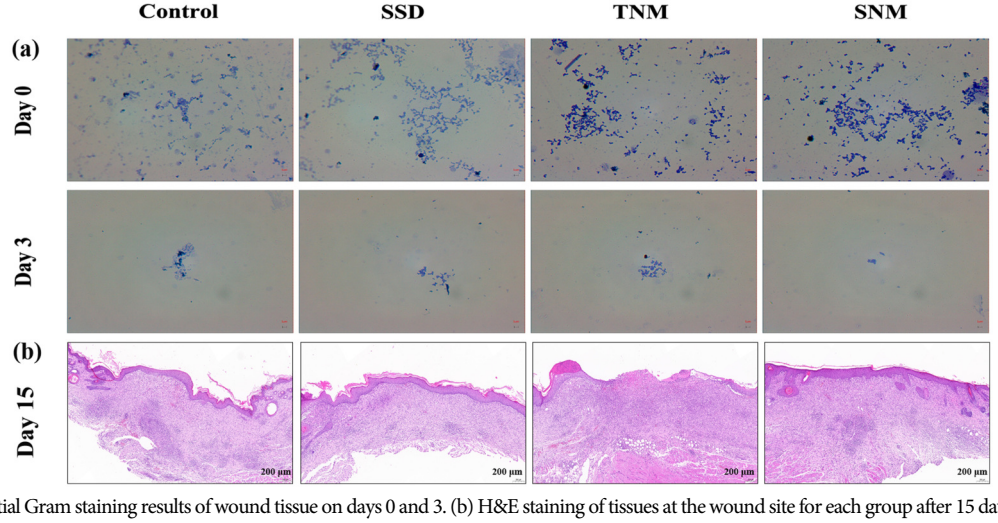

Figure 8 (a) The initial Gram staining results of wound tissue on days 0 and 3. (b) H&E staining of tissues at the wound site for each group after 15 days of treatment.

4 Experimental

4.1 Materials

Bombyx mori cocoons and WPU were obtained from Hefei Yuanli Instrument Technology Co., Ltd. (China). Lithium bromide (99.9%), sodium carbonate (99.9%), zinc nitrate hexahydrate (99.9%) and 2-methylimidazole (98%) were procured from Shanghai Macklin Biochemical Technology Co., Ltd. (China). Silver nitrate (analytical reagent (AR)) was obtained from Sinopharm Chemical Reagent Co., Ltd. (China), while EGCG (98%) was purchased from Shanghai Dibai Biotechnology Co., Ltd. (China). The PVA-SbQ solution (15% solid content, 1700 degree of polymerization, and 0.03–0.05 mol/kg SbQ) was purchased from Shanghai Guangyi Printing Technology Co., Ltd. (China).

4.2 Characterization

FTIR (Nicolet iS50), XRD (D8 ADVANCE), and XPS (ESCALAB Qxi) were employed to comprehensively analyze the chemical structures of the as-prepared material. Thermal stability was assessed using TGA (METTLER-TGA2). Microstructural analysis was performed using SEM (S4800) and TEM (JEM-2100PLUS). Elemental mapping of Ag-ZIF was conducted on an STEM (Talos F200X G2). Mechanical properties were determined using a microcomputer-controlled universal testing machine (MTS E44.304). Surface wettability was evaluated by measuring the WCA with an optical contact angle meter (Theta Flow). The DPPH radical scavenging efficiency was quantified using a UV–visible spectrophotometer (UV–vis, UV-2700i).

4.3 Synthesis of Ag-ZIF NPs

Ag-ZIF NPs were synthesized following a modified procedure reported by Jafar Abdi [51]. Initially, 1.17 g of zinc nitrate hexahydrate ($Zn(NO_3)_2{\cdot}6H_2O$) was dissolved in 8 g of deionized water. Separately, 22.7 g of H-MIM was dissolved in 80 g of deionized water. The $Zn(NO_3)_2$ solution was then slowly added dropwise to the H-MIM solution under continuous stirring. The resulting mixture was stirred for 2 h and aged for 24 h at room temperature to ensure complete reaction.

The resulting milky white solution, containing the synthesized ZIF-8 NPs, was centrifuged at 10,000 revolutions per minute (rpm) for 5 min. The precipitated nanoparticles were washed three times with deionized water to remove any unreacted precursors or impurities. The purified ZIF-8 NPs were then dried overnight in a vacuum oven at 60 °C. In the next step, 0.125 g of $AgNO_3$ was dissolved in 20 mL of deionized water. The solution was stirred for 15 min to ensure complete dissolution of the $AgNO_3$. Subsequently, 0.5 g of the previously prepared ZIF-8 NPs were added to the $AgNO_3$ solution. The mixture was then irradiated with a 300 W xenon lamp for 1 h to initiate the photoreduction of Ag ions onto the surface of the ZIF-8 NPs. The resulting Ag-ZIF NPs were separated from the solution by centrifugation at 10,000 rpm for 5 min. The precipitated NPs were washed three times with deionized water to remove any unreacted Ag ions or other impurities. Finally, the Ag-ZIF NPs were dried in a vacuum oven at 60 °C to remove any residual solvent.

4.4 Extraction of silk fibroin protein

Shredded *Bombyx mori* cocoons were degummed by soaking in a 0.5 wt.% sodium carbonate solution (liquid ratio 1:50) at 100 °C for 30 min, followed by rinsing with deionized water three times, and drying at room temperature for 24 h. The degummed silk was dissolved in a 9.3 M lithium bromide aqueous solution at 60 °C for 4 h (liquid ratio 1:4). The viscous solution was dialyzed against deionized water at 4 °C for 3 days, with the dialysis solution replaced 6 times within 48 h. Finally, the dialyzed solution was centrifuged at 9000 rpm for 20 min to obtain a silk fibroin solution. To determine the silk fibroin concentration, 1 mL of the solution was transferred to a glass vial, dried at 60 °C, and the weight percent of silk fibroin (wt.%) was calculated using the following equation (Eq. (1)):

$$\mathrm{SF\,(wt.\%)} = \frac{m_2 - m_1}{m_0} \times 100\% \tag{1}$$

where m_0, m_1, and m_2 represent the mass of 1 mL extraction solution, mass of the empty glass bottle, and the total mass of the glass bottle with silk fibroin protein after drying, respectively.

4.5 Fabrication of nanofiber membrane with a sandwich structure

Stock solutions (A, B, and C) were prepared in advance for electrospinning. Solution A was obtained by mixing 8 wt.% PVA and 35 wt.% WPU aqueous solution in a 1:1 mass ratio and stirring at room temperature for 12 h. To prepare solution B and C, PVA-SbQ and SF were mixed in a 5:1 mass ratio, followed by the addition of 5 wt.% Ag-ZIF (solution B) or 5 wt.% EGCG (solution C) and subsequent ultrasonication for uniform dispersion. A SNM was fabricated by electrospinning, employing WP as the outer layer, PSA as the middle layer, and PSE as the inner layer. The electrospinning parameters were as follows: needle diameter 20 G, voltage +15 kV/−1 kV, flow rate 0.48 mL/h. The resulting SNM were then vacuum-dried at 40 °C for 12 h.

4.6 Water vapor transmission rate

To accurately evaluate the moisture permeability of electrospun nanofiber membranes, this work strictly adhered to the standard procedure outlined by the American Society for Testing and Materials (ASTM). The WP, PSA, PSE, and SNM materials were cut into 4.0 cm × 4.0 cm squares and affixed to centrifuge tubes containing deionized water (inner diameter of 2.5 cm). The edges of the samples and tubes were sealed with tape to ensure airtight conditions. Control groups, consisting of unsealed centrifuge tubes, were also prepared. All sample groups were incubated 37 ± 3 °C and 50% ± 5% (relative humidity). The total weight of each sample and test tube was measured thrice (n = 3), and the measurement was repeated three times (n = 3). The WVTR of each sample group was calculated within 24 h according to the following equation (Eq. (2)):

$$\mathrm{WVTR} = \frac{M_0}{S \times T} \tag{2}$$

where M_0 denotes the initial total weight of the test sample and tube, S is the test area (with an inner diameter of 2.5 cm), and T denotes the incubation time.

4.7 Swelling properties of the integrated nanofiber membranes

In this study, the samples were cut into a size of 2 cm × 2 cm. After being kept at 25 °C with a relative humidity of 65% for a certain

period of time, the samples were weighed and recorded as m_0. Subsequently, the dressings were placed in a phosphate-buffered saline (PBS) buffer solution that was 40 times their own weight. At different time points and at a temperature of 37 °C, the weight of the fibrous membrane was measured. Before each measurement, the samples were left to drain freely for 30 s. The wet weight of the samples was recorded as m_1. Finally, the swelling rate was calculated using the equation (Eq. (3)):

$$\text{Swelling ratio}\,(\%) = \frac{m_1 - m_0}{m_0} \times 100\% \quad (3)$$

4.8 Antioxidant activity of the integrated nanofiber membranes

The antioxidant capacity of EGCG, PSE, and SNM was evaluated by measuring their ability to scavenge DPPH· radicals, following a previously established protocol. EGCG and DPPH were initially dissolved in ethanol. Subsequently, 1 mL of EGCG at varying concentrations was mixed with 1 mL of 0.2 mM DPPH solution in separate experiments. Electrospun nanofiber membranes containing the equivalent amounts of EGCG were dispersed in ethanol suspensions, followed by adding 1 mL of DPPH solution to each group. An ethanol solution without the test sample served as the blank, while a DPPH solution without the test sample was used as the control. Subsequently, the mixtures were incubated in the dark for 30 min before spectrophotometric measurement of absorbance at 517 nm. The antioxidant activity, specifically the DPPH· radical scavenging activity, was calculated using the following equation (Eq. (4)):

$$\text{Antioxidant activity} = \left(1 - \frac{A_{\text{sample}} - A_{\text{blank}}}{A_{\text{control}}}\right) \times 100\% \quad (4)$$

where A_{sample}, A_{blank}, and A_{control} represent the absorbance values at 517 nm of the sample, blank, and control, respectively.

4.9 Antibacterial activity of the integrated nanofiber membranes

The antibacterial efficacy of the material was evaluated using the agar plate diffusion method. *Escherichia coli* (ATCC 25922) and *Staphylococcus aureus* (ATCC 6538) were selected as the test microorganisms. The following steps were undertaken in the experimental procedure: Firstly, the bacteria were prepared using Luria-Bertani (LB) medium, and the optical density (OD) of the bacterial suspension was adjusted to 0.4–0.5, corresponding to approximately 1×10^8 colony-forming units (CFU)/mL). 100 μL of the adjusted bacterial suspension was evenly spreaded onto the surface of the agar plate. The sterilized electrospun nanofiber membranes were cut into circular pieces with a diameter of 1 cm, and placed on an agar plate, ensuring tight contact with the plate. Then, the plate was incubated at 37 °C for a 24-h cultivation period. Finally, the presence and size of a zone of inhibition surrounding the membranes were observed and recorded to assess antibacterial activity. Furthermore, the antibacterial efficacy was quantified using a 2 cm × 2 cm square specimen. A 25 μL aliquot of the bacterial suspension was inoculated onto the sample and incubated for 30 min. Subsequently, the sample was immersed in 40 mL of physiological saline and agitated for 5 min to dislodge adherent bacteria. This treated solution was compared to a control group consisting of a bacterial suspension without the test material. A 100-fold dilution of a 1 mL aliquot of the treated solution was plated onto an agar plate. After a 24-h incubation period at 37 °C, the CFU were counted to determine the antibacterial activity.

4.10 *In vitro* cellular antioxidant assay of the integrated nanofiber membranes

This study evaluated the antioxidant capacity of different materials by assessing L929 cell viability in a high concentration H_2O_2-induced oxidative damage environment. L929 cells were seeded in a 96-well plate at 5000 cells per well and incubated for 24 h. The culture medium was then replaced with 100 μL of medium containing 400 μM H_2O_2 to simulate an oxidative stress environment. One group of cells was not exposed to any material as a control. Other groups were treated with TNM and SNM (5 mg/mL). Additionally, culture medium without cells served as the blank group, and normal culture medium was the control group. Each group had three replicate wells. After co-incubation for 2 h, cell viability was measured using the CCK-8 assay.

4.11 *In vitro* Ag ions release assay

The *in vitro* release of silver ions from fibrous membranes was quantified using inductively coupled plasma mass spectrometry (ICP-MS). For this experiment, dressing materials SNM, cut into 2.0 × 2.0 cm^2 pieces, were accurately weighed and immersed in 0.01 M PBS with a pH of 7.4. The release experiment was conducted at 37 °C under continuous shaking at 220 rpm. At predetermined time intervals (0.5, 1, 3, 6, 12, and 24 h), 1 mL aliquots of the release medium were collected for analysis using ICP-MS. To ensure the accuracy and reliability of the data, independent samples were used for each time point, and each time point had three parallel samples to avoid sampling interference. The cumulative release rate of silver ions was then calculated based on the data obtained from ICP-MS analysis.

4.12 Cytotoxicity assays

To evaluate the biocompatibility of the electrospun nanofiber membranes, the CCK-8 method was employed to ascertain its toxicity to mouse L929 fibroblasts. Prior to the experiment, the nanofiber membranes were sterilized on both sides under ultraviolet light for 20 min. Subsequently, 50 mg of the sterilized membranes were immersed in 5 mL of Dulbecco's Modified Eagle Medium (DMEM) and incubated at 37 °C for 24 h to prepare a 10 mg/mL leachate. Mouse L929 fibroblasts were seeded into a 96-well cell culture plate at a density of 5000 cells per well and treated with the membrane leachate. The cells were incubated at 37 °C with 5% CO_2 for 12, 24, 36, and 48 h. Following incubation, the culture medium was removed, and 100 μL of DMEM and 10 μL of CCK-8 reagent were added to each well. After a 4-h incubation period, the absorbance should be measured at 450 nm using an enzyme-linked immunosorbent assay (ELISA) reader to assess cell viability.

4.13 *In vivo* wound healing promotion capability of the of the integrated nanofiber membranes

A total of 20 male BALB/c mice, aged 4–5 weeks, were randomly divided into four groups (n = 5) and anesthetized with isoflurane. The dorsal hair of each mouse was removed, and a full-thickness skin wound with a diameter of approximately 10 mm was created on the back. The wound was inoculated with a 10 μL suspension of

S. aureus at approximately 1.0×10^5 CFU/mL to establish an infection model. The negative control group received no treatment and allowed to heal naturally. The positive control group was treated with commercial SSD dressings. The TNM and SNM groups were treated with TNM (WP/PSE) bilayer and SNM (WP/PSA/PSE) trilayer, cut into 2 cm × 2 cm squares. The dressings were changed every three days, and the wound healing was monitored by a digital photography on days 0, 3, 6, 9, 12, 15, and 18. The wound areas were quantified using the ImageJ software. At the end of the 18-day treatment period, the mice were euthanized.

4.14 Gram staining experiment

In this experiment, mouse skin wound exudate samples were processed as follows. First, the samples were spread onto microscope slides and fixed by passing them back and forth through a flame three times at a constant speed. After the slides were cooled, 1 or 2 drops of crystal violet stain were added. The slides were then left to stain for 1 min. Next, free stain was washed away by running water starting from one end of the slide. After gently shaking off excess water, Lugol's iodine solution was added for 1 min, then the stain was poured off and the slide was rinsed with water until the runoff was colorless. Finally, the slides were air-dried and examined under an oil immersion lens.

4.15 Histological analysis

H&E staining was performed to examine the microscopic features of wound healing. On day 15, skin tissue samples from the wound-healing sites of mice were collected. The tissue sections were fixed in 4% formaldehyde solution for 24 h and then embedded in paraffin. Sections with a thickness of 5 μm were cut. The samples were subjected to dewaxing in xylene and rehydration with a descending series of ethanol (100%, 70%, and 60%) and water for 5 min. For H&E staining, the sections were first stained with hematoxylin and then with eosin solution. Finally, the stained tissue sections were examined under an optical microscope to analyze the histological changes during the wound-healing process.

4.16 Statistical analysis

All of the experiments were performed in triplicate. The data are expressed as the mean ± standard deviation. Statistical significance was assessed using Student's t-test, and the values were considered to be significant at $^*P \le 0.05$, $^{**}P \le 0.01$, and $^{***}P \le 0.001$.

Electronic Supplementary Material: Supplementary material (the particle size distribution of Ag-ZIF NPs, fiber diameter histogrtograms of SNM membranes, XRD patterns, stress-strain curves of SNM composites and other characterization results) is available in the online version of this article at https://doi.org/10.26599/NR.2025.94907385.

Data availability

Data will be made available on request.

Acknowledgements

This study was supported by the National Natural Science Foundation of China (NSFC) (Nos. 52273058, and 52073124), Natural Science Foundation of Jiangsu Province (No. BK2022030167), Wuxi Taihu Talent Training Project (Double hundred Medical Youth Professionals Program, No. BJ2023059), Young Elite Scientists Sponsorship Program by CAST (No. YESS20220554), Young Elite Scientists Sponsorship Program by Beijing association for science and technology (No. BYESS2024297), and the Fundamental Research Funds for the Central Universities (No. KYCX23_2465). The authors would also like to thank the Central Laboratory, School of Chemical and Material Engineering, Jiangnan University.

Declaration of competing interest

The authors declare that they have no known competing financial interests or personal relationships that could have appeared to influence the work reported in this paper.

Author contribution statement

H. Z.: Project administration, funding acquisition, manuscript revision, experimental design. H. X. Z.: Experimental design, data curation, writing manuscript. H. H: Data curation, data analysis. Y. Y. L.: Data curation, validation, data analysis. W. J. C.: Data analysis. J. X. A.: Data analysis. Y. Z.: Data analysis. M. L. D. Supervision; C. Y. J.: Dunding acquisition, manuscript revision. J. F. H.: Project administration, funding acquisition. All authors have approved the final manuscript.

Informed consent

Not applicable.

Ethics statement

The animal experiments were carried out following the guidelines of Jiangsu Institute of Parasitic Diseases and Use of Laboratory Animals and were approved by the Committee on Ethical Use of Animals of Jiangsu Institute of Parasitic Diseases (Ethical code: JIPD-2024-022).

Use of AI statement

None.

References

[1] Peña, O. A.; Martin, P. Cellular and molecular mechanisms of skin wound healing. *Nat. Rev. Mol. Cell. Biol.* **2024**, *25*, 599–616.
[2] Ji, Z. X.; Wei, T.; Zhu, J. F.; Hu, J. Y.; Xiao, Z. S.; Bai, B. X.; Lv, X. Y.; Miao, Y.; Chen, M. C.; Wang, C. et al. Actively contractible and antibacterial hydrogel for accelerated wound healing. *Nano Res.* **2024**, *17*, 7394–7403.
[3] Li, M. X.; Xia, W. Z.; Khoong, Y. M.; Huang, L. J.; Huang, X.; Liang, H.; Zhao, Y.; Mao, J. Y.; Yu, H. J.; Zan, T. Smart and versatile biomaterials for cutaneous wound healing. *Biomater. Res.* **2023**, *27*, 87.
[4] Kamoun, E. A.; Kenawy, E. R. S.; Chen, X. A review on polymeric hydrogel membranes for wound dressing applications: PVA-based hydrogel dressings. *J. Adv. Res.* **2017**, *8*, 217–233.
[5] Kokabi, M.; Sirousazar, M.; Hassan, Z. M. PVA-clay nanocomposite hydrogels for wound dressing. *Eur. Polym. J.* **2007**, *43*, 773–781.
[6] Wang, G.; Yang, F. F.; Zhou, W. Y.; Xiao, N. Y.; Luo, M.; Tang, Z. H. The initiation of oxidative stress and therapeutic strategies in wound healing. *Biomed. Pharmacother.* **2023**, *157*, 114004.

[7] Sun, Z. P.; Ding, Y. L.; Wang, Z. T.; Luo, H. T.; Feng, Q.; Cao, X. D. Ros-responsive hydrogel with size-dependent sequential release effects for anti-bacterial and anti-inflammation in diabetic wound healing. *Chem. Eng. J.* **2024**, *493*, 152511.

[8] Fang, M. K.; Zhang, H.; Wang, Y. Z.; Zhang, H.; Zhang, D. G.; Xu, P. P. Biomimetic selenium nanosystems for infectious wound healing. *Eng. Regener.* **2023**, *4*, 152–160.

[9] Kumar, G.; Khan, F. G.; Abro, M. I.; Aftab, U.; Jatoi, A. W. Development of cellulose acetate/CuO/AgNP nanofibers based effective antimicrobial wound dressing. *Compos. Commun.* **2023**, *39*, 101550.

[10] Che, P.; Liu, W.; Chang, X. X.; Wang, A. H.; Han, Y. S. Multifunctional silver film with superhydrophobic and antibacterial properties. *Nano Res.* **2016**, *9*, 442–450.

[11] Altman, G. H.; Diaz, F.; Jakuba, C.; Calabro, T.; Horan, R. L.; Chen, J. S.; Lu, H.; Richmond, J.; Kaplan, D. L. Silk-based biomaterials. *Biomaterials* **2003**, *24*, 401–416.

[12] Mazurek, Ł.; Szudzik, M.; Rybka, M.; Konop, M. Silk fibroin biomaterials and their beneficial role in skin wound healing. *Biomolecules* **2022**, *12*, 1852.

[13] Liu, J.; Xie, X, S.; Wang, T.; Chen, H.; Fu, Y. H.; Cheng, X. Y.; Wu, J. B.; Li, G.; Liu, C. M.; Liimatainen, H. et al. Promotion of wound healing using nanoporous silk fibroin sponges. *ACS Appl. Mater. Interfaces.* **2023**, *15*, 12696–12707.

[14] Kong, B.; Liu, R.; Cheng, Y.; Cai, X. D.; Liu, J. Y.; Zhang, D. G.; Tan, H.; Zhao, Y. J. Natural biopolymers derived hydrogels with injectable, self-healing, and tissue adhesive abilities for wound healing. *Nano Res.* **2023**, *16*, 2798–2807.

[15] Luo, H.; Yang, J. Y.; Xiang, Z.; Shi, R.; Chen, Y. Functional electrospinning Janus dressings with asymmetric surface wettability. *Appl. Mater. Today* **2024**, *41*, 102445.

[16] Xu, S. X.; Du, C.; Zhang, M. M.; Wang, R. Y.; Feng, W.; Wang, C. W.; Liu, Q. S.; Zhao, W. Electroactive and antibacterial wound dressings based on $Ti_3C_2T_x$ MXene/poly(ε-caprolactone)/gelatin coaxial electrospun nanofibrous membranes. *Nano Res.* **2023**, *16*, 9672–9687.

[17] Li, H. Y.; Zhang, Z. W.; Godakanda, V. U.; Chiu, Y. J.; Angkawinitwong, U.; Patel, K.; Stapleton, P. G.; de Silva, R. M.; de Silva, K. M. N.; Zhu, L. M. et al. The effect of collection substrate on electrospun ciprofloxacin-loaded poly(vinylpyrrolidone) and ethyl cellulose nanofibers as potential wound dressing materials. *Mater. Sci. Eng. C* **2019**, *104*, 109917.

[18] Anjum, F.; Agabalyan, N. A.; Sparks, H. D.; Rosin, N. L.; Kallos, M. S.; Biernaskie, J. Biocomposite nanofiber matrices to support ECM remodeling by human dermal progenitors and enhanced wound closure. *Sci. Rep.* **2017**, *7*, 10291.

[19] Park, H.; Patil, T. V.; Deb Dutta, S.; Lee, J.; Ganguly, K.; Randhawa, A.; Kim, H.; Lim, K. T. Extracellular matrix-bioinspired anisotropic topographical cues of electrospun nanofibers: A strategy of wound healing through macrophage polarization. *Adv. Healthc. Mater.* **2024**, *13*, 2304114.

[20] Guo, K. N.; Ou, K. K.; Amin Newton, M. A.; Zhang, J.; Xu, H.; Li, J. Y.; Xin, B. J.; Huang, Y. J. Multifunctional Janus nanofibrous membrane with unidirectional water transport and pH-responsive color-changing for wound dressing. *J. Colloid Interface Sci.* **2025**, *679*, 723–736.

[21] Liu, N.; Zhang, J.; Wang, Y. H.; Zhu, Q. J.; Wang, C. L.; Zhang, X.; Duan, J. Z.; Hou, B. R.; Sheng, J. L. Combination of metal-organic framework with Ag-based semiconductor enhanced photocatalytic antibacterial performance under visible-light. *Colloids Surf. A: Physicochem. Eng. Aspects* **2022**, *644*, 128813.

[22] Attwa, M.; Said, A.; ElGamal, M.; El-Shaer, Y.; Elbasuney, S. Bespoke energetic zeolite imidazolate frameworks-8 (ZIF-8)/ammonium perchlorate nanocomposite: A novel reactive catalyzed high energy dense material with superior decomposition kinetics. *J. Inorg. Organomet. Polym. Mater.* **2024**, *34*, 387–400.

[23] Kohsari, I.; Shariatinia, Z.; Pourmortazavi, S. M. Antibacterial electrospun chitosan-polyethylene oxide nanocomposite mats containing ZIF-8 nanoparticles. *Int. J. Biol. Macromol.* **2016**, *91*, 778–788.

[24] Nordin, N. A. H. M.; Racha, S. M.; Matsuura, T.; Misdan, N.; Abdullah Sani, N. A.; Ismail, A. F.; Mustafa, A. Facile modification of ZIF-8 mixed matrix membrane for CO_2/CH_4 separation: Synthesis and preparation. *RSC Adv.* **2015**, *5*, 43110–43120.

[25] Barjasteh, M.; Mohsen Dehnavi, S.; Ahmadi Seyedkhani, S.; Yahya Rahnamaee, S.; Golizadeh, M. Synergistic wound healing by novel Ag@ZIF-8 nanostructures. *Int. J. Pharm.* **2022**, *629*, 122339.

[26] Chook, S. W.; Chia, C. H.; Chan, C. H.; Chin, S. X.; Zakaria, S.; Sajab, M. S.; Huang, N. M. A porous aerogel nanocomposite of silver nanoparticles-functionalized cellulose nanofibrils for SERS detection and catalytic degradation of rhodamine B. *RSC Adv.* **2015**, *5*, 88915–88920.

[27] He, J. R.; Qu, W.; Feng, Y.; Jiang, J. R.; Luo, J. M.; Wu, Y. Z.; Peng, L. M. Multiple synergistic antibacterial melamine-impregnated paper based on nano Ag-doped ZIF-8. *Chem. Eng. J.* **2024**, *493*, 152453.

[28] Zhou, J. S.; Lian, J.; Hou, L.; Zhang, J. C.; Gou, H. Y.; Xia, M. R.; Zhao, Y. F.; Strobel, T. A.; Tao, L.; Gao, F. M. Ultrahigh volumetric capacitance and cyclic stability of fluorine and nitrogen co-doped carbon microspheres. *Nat. Commun.* **2015**, *6*, 8503.

[29] Xiao, Y.; Sun, P. P.; Cao, M. H. Core-shell bimetallic carbide nanoparticles confined in a three-dimensional N-doped carbon conductive network for efficient lithium storage. *ACS Nano* **2014**, *8*, 7846–7857.

[30] Bahadur, A.; Shoaib, M.; Saeed, A.; Iqbal, S. FT-IR spectroscopic and thermal study of waterborne polyurethane-acrylate leather coatings using tartaric acid as an ionomer. *e-Polymers* **2016**, *16*, 463–474.

[31] Allayarov, S. R.; Confer, M. P.; Dixon, D. A.; Rudneva, T. N.; Kalinin, L. A.; Tolstopyatov, E. M.; Frolov, I. A.; Ivanov, L. F.; Grakovich, P. N.; Golodkov, O. N. Effect of initial γ-irradiation on infrared laser ablation of poly (vinyl alcohol) studied by infrared spectroscopy. *Polym. Degrad. Stab.* **2020**, *181*, 109331.

[32] Zaman, H. U.; Islam, J. M. M.; Khan, M. A.; Khan, R. A. Physico-mechanical properties of wound dressing material and its biomedical application. *J. Mech. Behav. Biomed. Mater.* **2011**, *4*, 1369–1375.

[33] Farshi, P.; Salarian, R.; Rabiee, M.; Alizadeh, S.; Gholipourmalekabadi, M.; Ahmadi, S.; Rabiee, N. Design, preparation, and characterization of silk fibroin/carboxymethyl cellulose wound dressing for skin tissue regeneration applications. *Polym. Eng. Sci.* **2022**, *62*, 2741–2749.

[34] Idumah, C. I.; Obele, C. M. Understanding interfacial influence on properties of polymer nanocomposites. *Surf. Interfaces* **2021**, *22*, 100879.

[35] Deng, Y. X.; Zhang, Q.; Qu, D. H. Emerging hydrogen-bond design for high-performance dynamic polymeric materials. *ACS Mater. Lett.* **2023**, *5*, 480–490.

[36] Bai, H. Y.; Sun, Y. L.; Xu, J.; Dong, W. F.; Liu, X. Y. Rheological and structural characterization of HA/PVA-SbQ composites film-forming solutions and resulting films as affected by UV irradiation time. *Carbohydr. Polym.* **2015**, *115*, 422–431.

[37] Bai, H. Y.; Chen, D. W.; Zhu, H. Y.; Zhang, S. W.; Wang, W.; Ma, P. M.; Dong, W. F. Photo-crosslinking ionic conductive PVA-SbQ/$FeCl_3$ hydrogel sensors. *Colloids Surf. A: Physicochem. Eng. Aspects* **2022**, *648*, 129205.

[38] Wu, P.; Fisher, A. C.; Foo, P. P.; Queen, D.; Gaylor, J. D. S. *In vitro* assessment of water vapour transmission of synthetic wound dressings. *Biomaterials* **1995**, *16*, 171–175

[39] Yue, Y. P.; Gong, X. B.; Jiao, W. L.; Li, Y.; Yin, X.; Si, Y.; Yu, J. Y.; Ding, B. *In-situ* electrospinning of thymol-loaded polyurethane fibrous membranes for waterproof, breathable, and antibacterial wound dressing application. *J. Colloid Interface Sci.* **2021**, *592*, 310–318.

[40] Liu, X. Z.; Li, L. X.; Wang, M.; Zhang, B. B. Robust ZIF-8 based superhydrophobic coating with anti-icing, anti-corrosion, and substrate universality. *J. Ind. Eng. Chem.* **2024**, *144*, 679–690.

[41] Janjhi, F. A.; Chandio, I.; Janwery, D.; Vatanpour, V.; Castro-Muñoz, R. A review on hydrophobic electrospun nanofibers-based materials and membranes for water treatment: Challenges, outlook, and stability. *Sep. Purif. Technol.* **2025**, *353*, 128370.

[42] Tan, S. J.; Han, J. R.; Yuan, X. N.; Song, Z. Y.; Gao, L. H.; Gao, J.; Wang, L. Epigallocatechin gallate-loaded pH-responsive dressing with effective antioxidant, antibacterial and anti-biofilm properties for wound healing. *Mater. Des.* **2023**, *227*, 111701.

[43] Pang, Y. P.; Zhao, M. F.; Xie, Y. H.; Wang, Y. P.; You, Y. X.; Ke, Y. D.; Zhang, C. Y.; Chen, X. H.; Yang, Y. J.; Zhang, C. L. et al. Multifunctional Ac@ZIF-8/AgNPs nanoplatform with pH-responsive and ROS scavenging antibacterial properties promotes infected wound healing. *Chem. Eng. J.* **2024**, *489*, 151485.

[44] Kędziora, A.; Speruda, M.; Krzyżewska, E.; Rybka, J.; Łukowiak, A.; Bugla-Płoskońska, G. Similarities and differences between silver ions and silver in nanoforms as antibacterial agents. *Int. J. Mol. Sci.* **2018**, *19*, 444.

[45] Zhu, Y.; Xu, J.; Wang, Y. M.; Chen, C.; Gu, H. C.; Chai, Y. M.; Wang, Y. Silver nanoparticles-decorated and mesoporous silica coated single-walled carbon nanotubes with an enhanced antibacterial activity for killing drug-resistant bacteria. *Nano Res.* **2020**, *13*, 389–400.

[46] Yuan, X.; Setyawati, M. I.; Leong, D. T.; Xie, J. P. Ultrasmall Ag^{+}-rich nanoclusters as highly efficient nanoreservoirs for bacterial killing. *Nano Res.* **2014**, *7*, 301–307.

[47] Zheng, H. Y.; Zhong, B. Y.; Wang, Q. W.; Li, X.; Chen, J. H.; Liu, L.; Liu, T. T. ZnO-doped metal-organic frameworks nanoparticles: Antibacterial activity and mechanisms. *Int. J. Mol. Sci.* **2023**, *24*, 12238.

[48] Zhang, Y. M.; Zhang, X.; Song, J.; Jin, L. M.; Wang, X. T.; Quan, C. S. Ag/H-ZIF-8 nanocomposite as an effective antibacterial agent against pathogenic bacteria. *Nanomaterials* **2019**, *9*, 1579.

[49] Liu, J. H.; Wu, D.; Zhu, N.; Wu, Y. N.; Li, G. L. Antibacterial mechanisms and applications of metal-organic frameworks and their derived nanomaterials. *Trends Food Sci. Technol.* **2021**, *109*, 413–434.

[50] López-García, J.; Lehocký, M.; Humpolíček, P.; Sáha, P. HaCaT keratinocytes response on antimicrobial atelocollagen substrates: Extent of cytotoxicity, cell viability and proliferation. *J. Funct. Biomater.* **2014**, *5*, 43–57.

[51] Abdi, J. Synthesis of Ag-doped ZIF-8 photocatalyst with excellent performance for dye degradation and antibacterial activity. *Colloids Surf. A: Physicochem. Eng. Aspects* **2020**, *604*, 125330.